Progressive Failure Characteristics and Failure Symptoms of Straight-Walled Arched Sandstone Tunnels

Peiyuan Xu[1], Liming Zhang[1]*, Jinyu Zhang[2], Jianxin Wang[3], Sulei Zhang[1], Pengchu Zhang[1]

[1] School of Civil Engineering, Qingdao University of Technology, 266033 Qingdao, Shandong, China
[2] Qingdao Engineering Company Ltd of China Railway 10th Group, 266011 Qingdao, Shandong, China
[3] National Institute of Natural Hazards, Ministry of Emergency Management of China, 100085 Beijing, China

* Correspondence: Liming Zhang (shzhlm@qtec.edu.cn)

Abstract: In order to investigate the development process of crack formation in shallow-buried sandstone tunnel, biaxial compression tests were conducted on a similar model of the real straight-walled arched sandstone tunnel. The results indicate that the initial crack appeared at the arch line on both sides of the tunnel and propagated downwards, eventually leading to spalling of the rock mass on the surface of the tunnel, forming a V-shaped groove. Additionally, slab cracks were observed in the straight wall on the right side of the tunnel, which were approximately parallel to the vertical load. The failure characteristics of the tunnel were closely related to the fractal dimension of the crack geometry distribution. During the tunnel compaction and elastic deformation stage, the fractal dimension of the cracks in the tunnel surface increased linearly, while during the crack propagation stage, the fractal dimension increased gradually, with a sudden increase occurring just before the rock mass reached its peak load. The acoustic emission results revealed that AE ringing counts and amplitude were inactive during the first 4239 seconds of the test. And they only increased during the crack propagation stage. The continuous decrease of the *b*-value and the sudden increase of the fractal dimension of cracks can serve as a reliable precursor of tunnel failure.

Keywords: Straight-walled arched tunnel; Sandstone; Fractal analysis; Acoustic emission; Failure

1. Introduction

With the development of China's economy, the scale of underground space development is gradually increasing, leading to an increase in the construction of tunnel engineering [1]. Tunnel failure tests are widely used to analyze the tunnel deformation process and identify the most dangerous positions Circular and straight-walled arched tunnels are common types of tunnels used in tunnel engineering. Previous studies have conducted physical model tests on straight-walled arched tunnels, using different sample sizes and materials. Zhang et al. [2] conducted biaxial tests on circular sandstone tunnels with dimensions of 500mm × 500mm × 200mm. They found that the circular tunnel first developed tensile cracks at the arch haunch, followed by shear cracks on both sides of the opening, and finally, the tensile-shear cracks on both sides of the tunnel developed to the top. Gong et al. [3] applied true triaxial tests on straight-walled arched sandstone tunnels with dimensions of 100mm × 100mm × 100mm. They observed that the failure of the straight-walled arched tunnel mainly occurred between the two arch feet and the arch haunch, showing typical tensile plate fracture characteristics. Zhang et al. [4] conducted uniaxial compression tests on 100mm × 100mm × 100mm Straight-Wall-Top-Arch Roadway. They found that the straight-walled arched tunnel exhibited splitting rock burst phenomenon, and the surrounding rock fracture surface had undulating, rough features, and the surrounding rock was split into thin blocks. Zhou et al. [5] used similar material models of straight-walled arched structures of different sizes. They found that the crack surface of the side wall was approximately parallel to the tunnel wall, while the crack surface of the arch haunch and arch foot is at a certain angle to the tunnel wall. Pan et al. [6] conducted loading tests on straight-walled arched tunnels in red sandstone with different filling materials. They found that the straight-walled side of the tunnel without cracks

experienced an approximately symmetrical peeling failure, while the tunnel with prefabricated cracks exhibited asymmetric brittle failure. These studies demonstrate that the sample size significantly affects the crack development characteristics and failure rate of tunnels.

The expansion of internal cracks in tunnels generates stress waves, and acoustic emission contains rich information about the internal microcrack activity of tunnels. Chmel and Shcherbakov [7] believed that acoustic emission phenomena can well reflect the development process of internal rock cracks. Hu et al. [8] used acoustic emission monitoring and ultrasonic testing technology to study the rock damage evolution during tunnel boring machine (TBM) excavation. They classified the surrounding rock with different degrees of damage into loose zone, damage zone, and disturbance zone. Kim et al. [9] considered that acoustic emission technology can determine the cracking stress and damage stress of rocks. Das et al. [10] conducted uniaxial compression tests on tunnel experiments, and the results showed that acoustic emission technology can analyze and predict the brittle failure of tunnels.

Although scholars have made fruitful achievements in the study of tunnel damage, previous studies generally used small-sized real rock models in tunnel model tests, with sample sizes not exceeding 200mm. Tunnel model tests with sizes larger than 500mm all used similar materials such as cement and gypsum, lacking the failure test of larger-sized real rock tunnels. This article conducted biaxial compression tests and acoustic emission monitoring on a 500mm high straight-walled arched sandstone tunnel. The tunnel failure process was visually recorded with a high-speed camera, and the crack expansion process of the straight-walled arched tunnel was interpreted. Fractal theory was used to quantitatively describe the crack expansion process, and tunnel failure precursors were explored through the acoustic emission and fractal dimension.

In summary, this study's findings contribute to the understanding of the crack expansion process of straight-walled arched tunnels and provide a quantitative method for analyzing the crack expansion process through fractal theory. The study also highlights the importance of conducting tunnel failure tests on larger-sized real rock tunnels to better understand the distribution of crack patterns in different tunnels sizes.

2. Experimental Plan Design for Straight-Walled Arched Tunnels

2.1 Model Preparation

At an underground cavern site, a large, naturally weathered sandstone block was manually excavated and processed into a straight-walled arched tunnel model at a stone factory. The model's dimensions are 450mm x 500mm x 100mm, with a cross-section scaled down according to the actual proportion of the straight-walled arched tunnel. A straight-walled arched hole that penetrates the sample was cut into the model using a water jet, with a semi-circular arch radius of 40mm, straight wall height of 80mm, and a bottom length of 80mm, as shown in Figure 1. The geometric similarity constant of the model test is 1/125. Indoor testing revealed that the compressive strength of sandstone standard cylindrical specimens was 27MPa, the elastic modulus was 7.8GPa, the density was 2350kg/m^3, and the wave velocity was 2540m/s.

<div align="center">

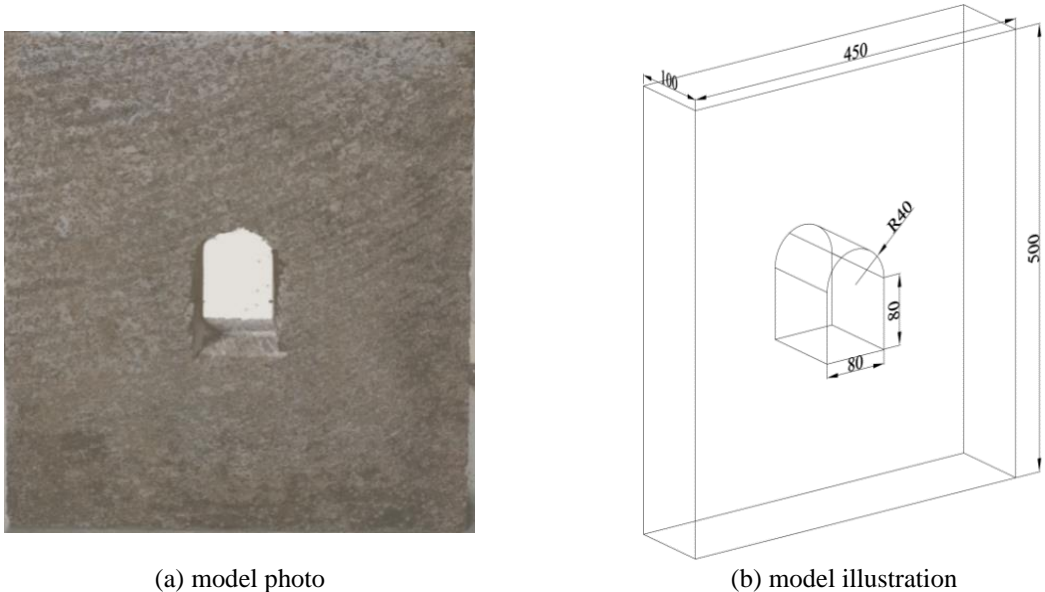(a) model photo   (b) model illustration

Figure 1. Straight-walled arched sandstone tunnel model

</div>

2.2 Loading Equipment and Observation Devices

The experiment was performed using a modified rock triaxial testing machine that provides a maximum axial force of 2000kN and real-time monitoring of the load and deformation information of the tunnel. Steel pressure plates were placed on both sides of the tunnel model and connected to hydraulic pumps for applying confining pressure to the tunnel. To ensure uniform force distribution on the tunnel model, steel plates with dimensions of 800mm x 300mm x 30mm were placed on the top and bottom of the tunnel. Additionally, all steel plates and the four side walls of the tunnel were coated with a layer of vaseline oil to reduce frictional effects. The center of the vertical loading column of the testing machine was aligned with the center of the tunnel along a vertical line to prevent eccentric compression, as shown in Figure 2.

A high-speed camera was placed in front of the tunnel to record the experiment process at a speed of 1fps. The PCI-2 type acoustic emission equipment was used to monitor parameters such as ringing count and energy count during the deformation process of the tunnel. The acoustic emission threshold value was set at 32dB, the resonance frequency ranged from 20-400kHz, the preamplifier threshold value was 40dB, and the sampling frequency was 1MHz.
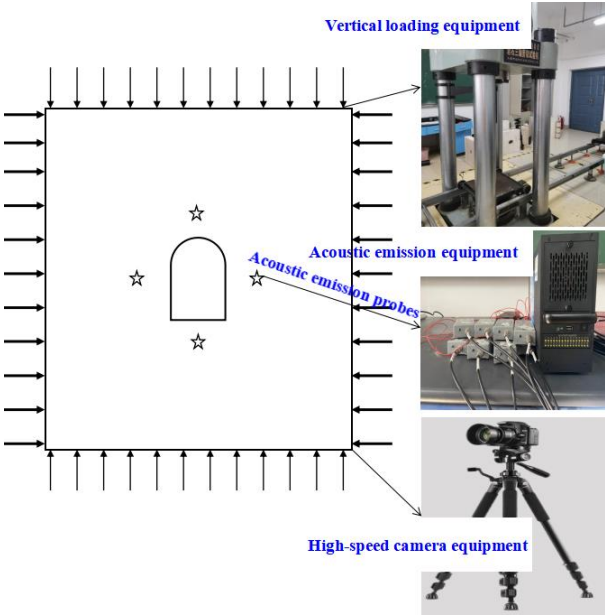

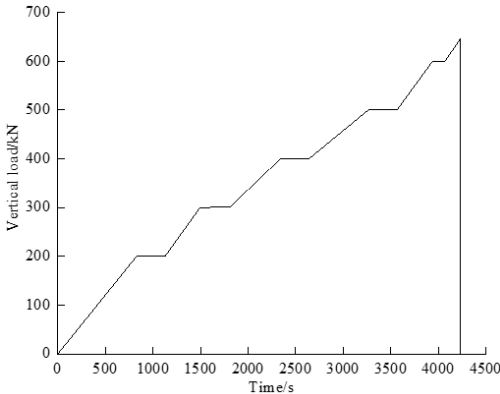**Figure 2.** Testing loading device

Figure 3. Biaxial loading test stress path

2.3 Loading Plan

To simulate the initial stress state and excavation depth of 100m, the tunnel is subjected to a confining pressure of 3MPa on both sides. The vertical load is applied in stages, as depicted in Figure 3. The maximum vertical load that the sandstone tunnel can withstand is approximately 700kN. The designed loading path for the vertical load F_z is as follows: stress-controlled loading is used to increase F_z to 200kN at a speed of 500N/s and maintain it for

300s. Displacement-controlled loading is used for staged loading, with F_z increasing by 100kN per level at a speed of 0.02mm/min. After each level of loading is completed, it is held constant for 300s, Then the loading continues until the tunnel is damaged. During the experiment, an acoustic emission collection system is implemented to record acoustic emission information.

3. Analysis of Experimental Results

3.1 Load-Deformation Curve Characteristics of the Tunnel

Figure 4 shows the relation between the vertical load and vertical deformation of the straight-walled arched tunnel. The deformation of the tunnel can be divided into four stages: pore closure (stage ab), elastic deformation (stage bc), crack propagation (stage cd), and post-peak drop (stage de) stages.
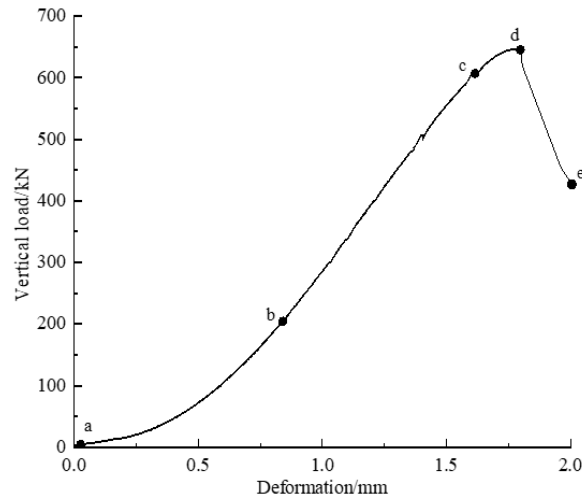

Figure 4. Load-deformation curve of the tunnel

The load-deformation curve of the tunnel can be classified into four stages. In the pore closure stage (stage ab), the original small pores inside the tunnel are gradually compressed, resulting in a concave-shaped load-deformation curve. In the elastic deformation stage (stage bc), the load-deformation curve shows linear behavior, and no visible new cracks appear on the tunnel's surface. In the crack propagation stage (stage cd), the load-deformation curve becomes non-linear from point c, with a slow increase in load and a convex curve. This stage is accompanied by the emergence of macroscopic cracks on the tunnel surface, which continue to expand until reaching the peak load point d. In the post-peak drop stage (stage de), the bearing capacity of the tunnel rapidly decreases, internal cracks penetrate through, the surface rock mass peels off, and large-scale damage occurs, accompanied by a loud noise. The deformation at the peak load is 1.8mm.

3.2 Crack Propagation Characteristics of the Tunnel Surface

The process of surface crack propagation in the sandstone tunnel was captured by a high-speed camera in Figure 5. At t = 4238s (F_z = 646.08kN), the tunnel surface showed no sign of cracks or peeling, and the rock pores were compressed, indicating the elastic deformation stage (stage bc). At t = 4239s (F_z = 646.14kN), the rock entered the crack propagation stage (stage cd), and a crack 1 appeared on the left spandrel sloping downward to the left, while an arc-shaped crack 2 opened downward on the right haunch due to high stress concentration caused by the slight curvature near the spandrel (Figure 5(b)). At t = 4240s (F_z = 646.27kN), the rock strength reached the peak load point d. The two haunches of the tunnel were subjected to tangential and compressive stresses. Although crack 1 on the left side did not change significantly, a small rock mass on the left side bulged, and crack 3 rapidly expanded from the right side of the arch foot along the edge wall to the upper right corner of the spandrel, causing tunnel to produce a tension crack rock fragment. Additionally, cracks 2 and 4 originating from the right haunch cut and peeled off the tunnel surface for the first time (Figure 5(c)). At t = 4241s (F_z = 123.79kN), the tunnel entered the post-peak drop stage (stage de). Although crack 1 did not change significantly, the rock mass on the right side of the tunnel continued to peel off above the already peeled rock mass, and the right side of the tunnel wall produced a curved deformation of the tensioned rock block that gradually separated from the tunnel wall (Figure 5(d)). At t = 4242s~4243s (F_z = 119.86kN100.91kN), crack 1 did not change significantly, while the peeled rock mass on the right side formed a "V-shaped groove," and the rock mass that peeled off from the right side of the tunnel wall

separated from the wall, resulting in brittle failure of the tunnel with a loud noise. Throughout the deformation process, plate crack failure gradually evolved and developed from the arch foot of the edge wall to the entire edge wall (Figure 5(e), (f)). The time for crack propagation to the tunnel failure was very short, only 2 seconds, indicating a significant suddenness in the tunnel failure.
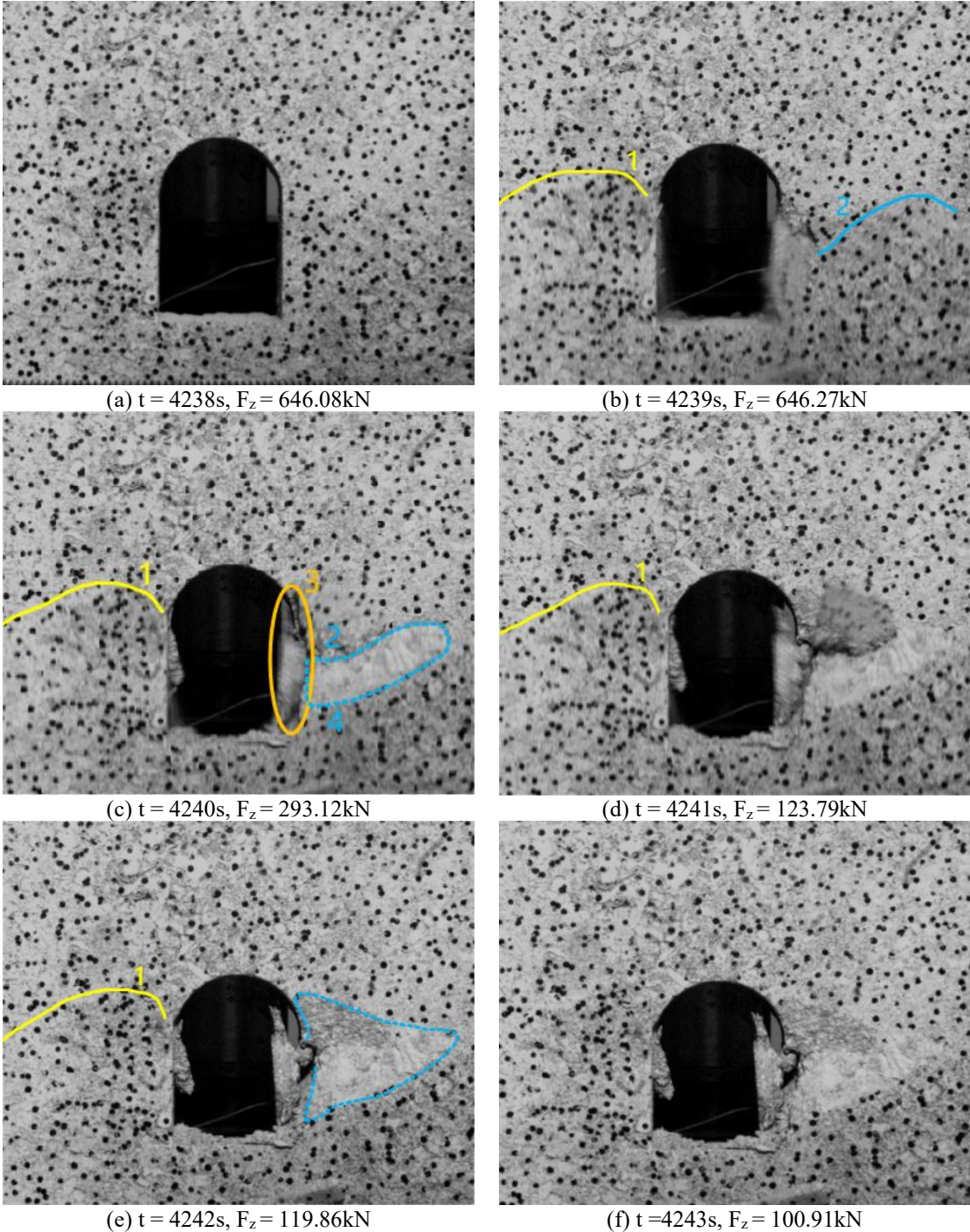
(a) t = 4238s, F_z = 646.08kN

(b) t = 4239s, F_z = 646.27kN

(c) t = 4240s, F_z = 293.12kN

(d) t = 4241s, F_z = 123.79kN

(e) t = 4242s, F_z = 119.86kN

(f) t = 4243s, F_z = 100.91kN

Figure 5. Process of surface crack propagation in the tunnel

3.3 Failure Characteristics of Tunnel

Following the failure of the sandstone tunnel, it was observed that the majority of the damage occurred in the straight wall areas on both sides, as depicted in Figure 6. A crack 1, sloping downward from the spandrel to the left, was present on the left side of the tunnel while on the right side of the opening, a crack 2 developed

horizontally after the rock mass peeled off. As the axial stress increased, the tunnel collapsed on the right side of the straight wall arch, indicating that defects in the tunnel experienced the most significant stress concentration under axial stress, with the ultimate failure caused by the combination of a V-shaped groove and shear cracks. The extent of damage to the straight walls on both sides of the tunnel varied; however, more severe damage was observed on the right side than on the left. The arch did not undergo significant damage, and a macro-sized crack appeared horizontally at the approximate center of the tunnel floor. The final outcome was the brittle failure of the straight wall arch tunnel, accompanied by a loud noise.
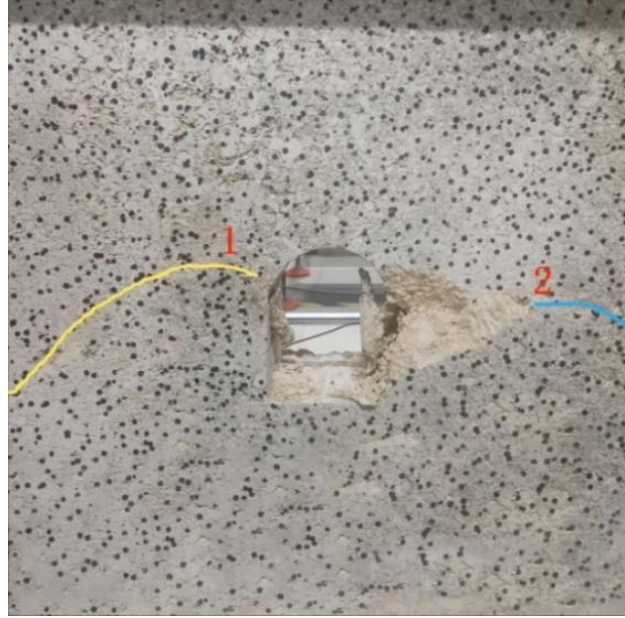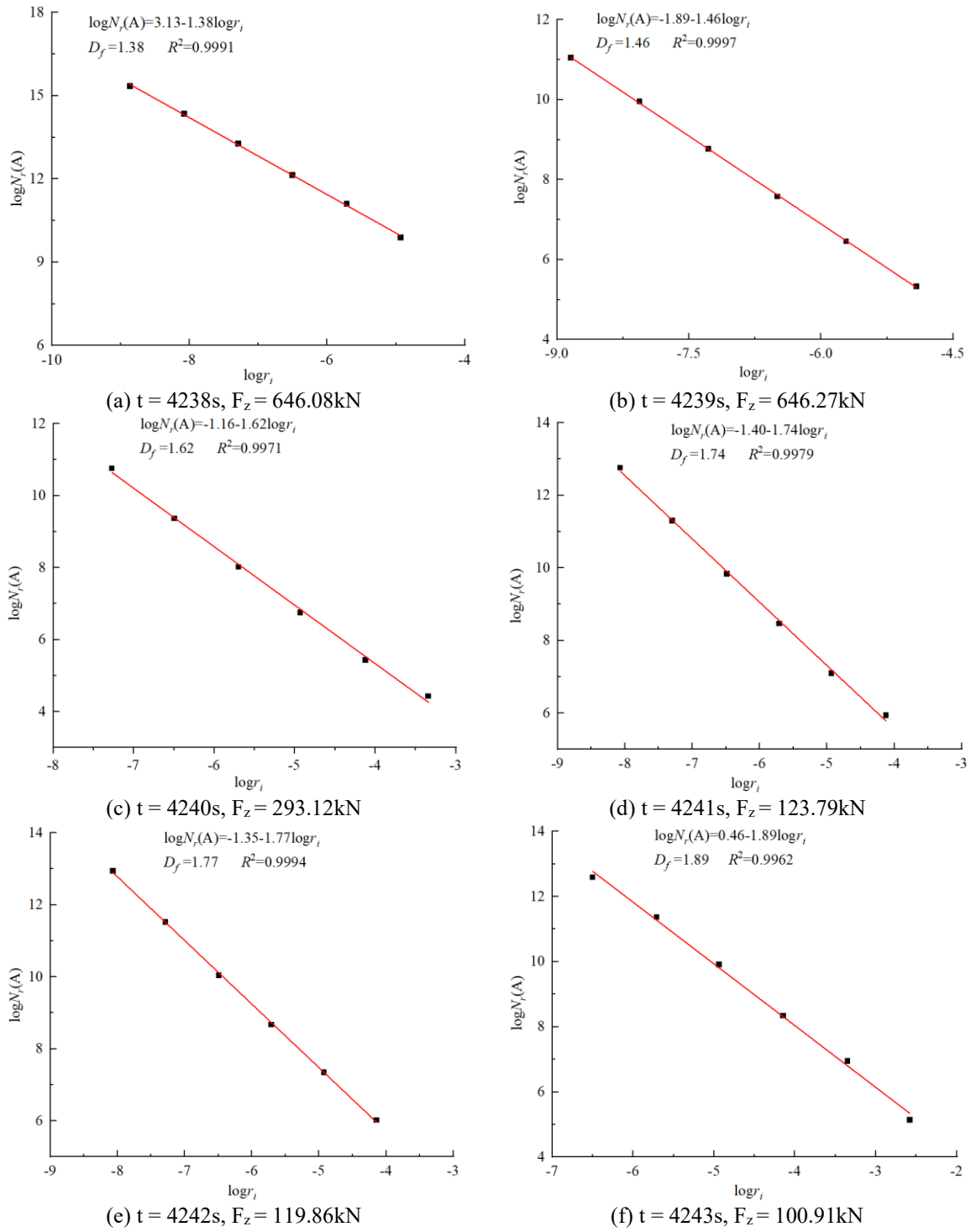

Figure 6. Photos of tunnel failure

3.4 Fractal Characteristics of Cracks in Tunnels' Surface

The path of crack propagation within the rock mass is complex under the external loads, and the fractal dimension is the most important parameter for describing fractal geometric characteristics. It can be used to quantitatively describe irregular phenomena. The box-counting method is used to calculate the fractal dimension of the crack propagation process. The principle involves covering the newly formed crack with a box of edge length r_i and calculating the required number N_i. When $r_i \rightarrow 0$, D_f is defined as the fractal dimension of the crack [11].

$$D_f = \lim_{r_i \rightarrow 0} \frac{\log N_r(A)}{\log r_i} \tag{1}$$

Surface cracks of the tunnel were extracted at different times, and a self-written MATLAB program was used to calculate the fractal dimension, as shown in Figure 7. The relationship between the square size r and the number of square cells N_i covered by the surface cracks of the tunnel at different times showed a good linear correlation, with the correlation coefficients greater than 0.996, indicating that the surface cracks of the tunnel have fractal characteristics. The fractal dimension gradually increased with the increase in the number of cracks.

Figure 8 shows the variation of the fractal dimension of the cracks during the tunnel deformation process, which exhibited period changes. During the pore closure and elastic deformation stages (I and II), the fractal dimension remained relatively stable, with a minimal increase from 0 to 0.03. The surface cracks of the tunnel were only distributed in small areas and were almost invisible to the naked eye. During the crack propagation stage (III), the fractal dimension showed a linear increase, with the value increasing from 0.03 to 1.62, as the tensile and shear cracks gradually expanded. A sudden change point (a) appeared in the fractal dimension during this stage, and the value increased from 1.62 to 1.77, corresponding to the peeling off of the right side of the tunnel and the expansion of the tunnel failure zone. During the post-peak stage (IV), only the tip of the right-side V-shaped groove crack extended downwards, and the fractal dimension increased slightly, with the value increasing from 1.77 to 1.89.

(a) t = 4238s, F$_z$ = 646.08kN   (b) t = 4239s, F$_z$ = 646.27kN

(c) t = 4240s, F$_z$ = 293.12kN   (d) t = 4241s, F$_z$ = 123.79kN

(e) t = 4242s, F$_z$ = 119.86kN   (f) t = 4243s, F$_z$ = 100.91kN

Figure 7. The values of the fractal dimension of surface cracks of the tunnel at different times
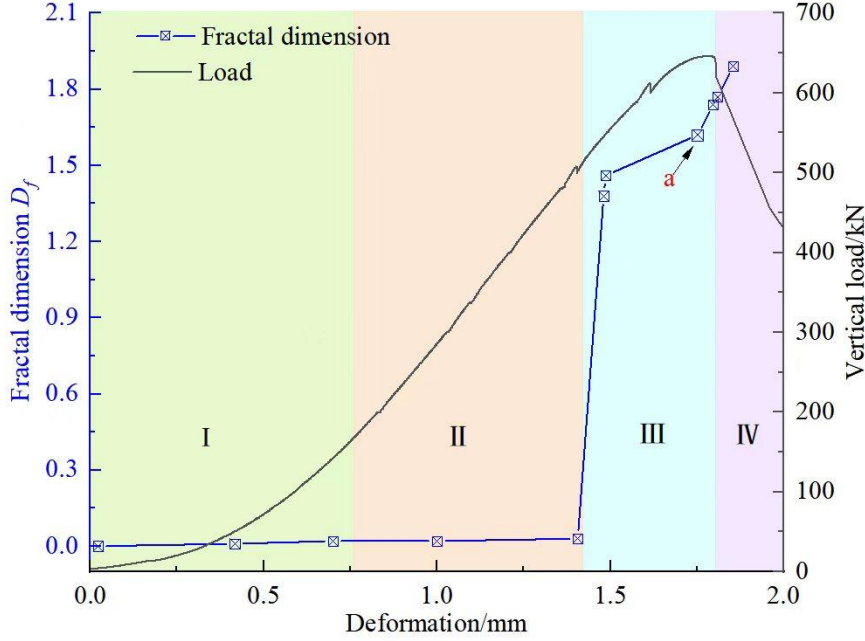
Figure 8. The relationship between fractal dimension and deformation of cracks

4. Acoustic Emission Monitoring Results

The curves of the acoustic emission ringing count and amplitude during the tunnel deformation process are presented in Figure 9 and Figure 10, with deformation represented by Δx.

During the initial loading stage, the acoustic emission activity was weak, and no macroscopic cracks appeared. Only during the crack propagation stage ($\Delta x = 1.77$ mm, $F_z = 645.86$ kN), the acoustic emission activity begins to increase, indicating that the expansion of microcracks inside the rock mass would intensify under higher loads.

At $\Delta x = 1.779$ mm ($F_z = 646.14$ kN), the ringing count of the acoustic emission showed the first surge (marked as ① in Figure 9 and Figure 10), gradually increasing to a maximum of 500 times. The amplitude of the acoustic emission fluctuated between 28-34 dB previously, but began to show an increasing trend, increasing from 32 dB to 62 dB. A new crack 1 extended downward at a 30° angle from the left spandrel of the tunnel, and an arc-shaped new crack 2 appeared on the right haunch (as shown in Figure 5(b)).

At $\Delta x = 1.781$ mm ($F_z = 646.27$ kN), the ringing count of the acoustic emission showed the second surge (marked as ② in Figure 9 and Figure 10), and the amplitude also showed an increasing trend, reaching a value of 66 dB. At this time, a crack appeared on the right shoulder of the tunnel, sloping downwards at a 30° angle. When the peak load was reached, the ringing count and amplitude of the acoustic emission reached the maximum value, with the ringing count reaching up to 3277 times and the amplitude reaching up to 70 dB. The crack 2 on the right haunch cut through the tunnel surface for the first time (as shown in Figure 5(c)).

During the peak load of $\Delta x = 1.782$ mm to 1.784 mm ($F_z = 293.12$ kN to 119.86 kN), the ringing count and amplitude of the acoustic emission sharply decreased. The rock mass on the right side of the tunnel's straight wall underwent peeling, the tunnel's sidewall underwent bending deformation, and the rock mass on the left side of the sidewall bulged, ultimately leading to brittle failure of the rock mass (as shown in Figure 5(d)).

4.1 Characteristic of Acoustic Emission b-Value

Acoustic emission is the phenomenon of acoustic waves detected during the energy release of rock deformation. By analyzing the seismic magnitude and the frequency-related parameter b-value [12, 13], the characteristics of the tunnel deformation and failure process can be studied. To calculate the b-value, every 100 acoustic emission events are set as a calculation segment, and the acoustic emission frequency N and the average energy value representing the magnitude are obtained for this time period [12].

$$b = \frac{\sum lgN_i \sum M_i - \Delta m \sum lgN_i \sum M_i}{\Delta m \sum M_i^2 - \left(\sum M_i\right)^2} \tag{2}$$

where, Δm is the interval between acoustic emission event classifications, with $\Delta m = 0.5$; M_i is the total number of acoustic emission events in the ith classification.
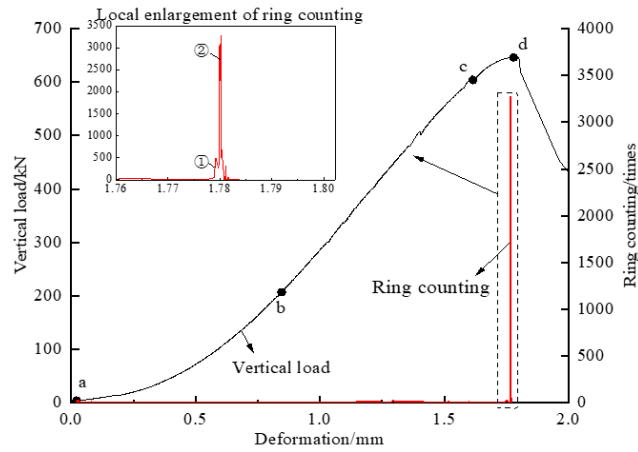
Figure 9. Ringing count-deformation curve

By applying the principle of calculating the b-value of acoustic emission, the variation of the b-value was obtained by setting every 100 acoustic emission events as a calculation segment, as shown in Figure 11. The b-value of acoustic emission fluctuated between 0.1 and 0.33 in an upward and downward trend. After entering the crack propagation stage (starting from point A in Figure 11), the b-value no longer increased but continuously decreased. This indicates that large-sized cracks have appeared inside the tunnel and are in an unstable propagation state. When the tunnel is damaged, the b-value of acoustic emission decreases to the lowest point of 0.05. Hence, it can be concluded that a sustained decrease in the b-value of acoustic emission indicates that the tunnel is about to be damaged.
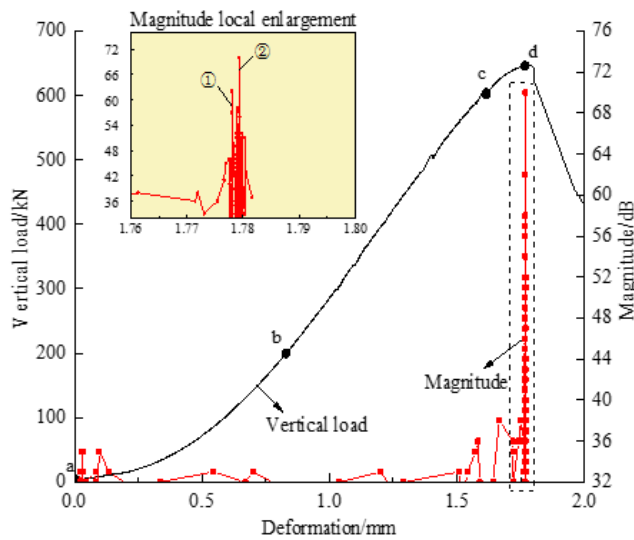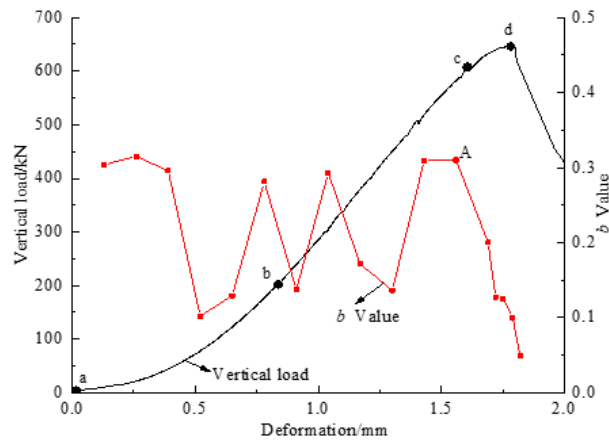

Figure 10. Amplitude-deformation curve

Figure 11. Acoustic emission *b*-value deformation curve

5. Discussion

5.1 Tunnel Failure Mechanism

During the tunnel excavation process, if the stress on the tunnel's straight wall exceeds the shear strength of the rock mass, it can cause compressive-shear type slip-line failure in the arch foot, sidewalls, and wall foot areas. This type of failure is shallow and only occurs near the sidewall [14, 15]. On the right side of the tunnel, the rock mass peels off, forming a "V-shaped groove" due to the separation of the surrounding rock and the tunnel wall caused by the cracking of the arch foot along the straight wall. The thickness of the peeled-off rock mass is around 3cm. The damage on the left side of the straight wall is relatively mild, with the cut rock block separating from the tunnel wall but not peeling off (as shown in Figure 12).

Based on the crack evolution process in the tunnel, tensile stress first concentrates on both sides of the straight wall. When the tensile stress exceeds the tensile strength of the rock mass, tensile cracks appear on both sides of the straight wall. As the distance to the tunnel boundary increases, the compressive stress on both sides of the tunnel gradually increases, and the compressive stress concentrates to form shear cracks [16]. As the load increases, penetrating cracks appear inside the surrounding rock, separating the cutting rock from the tunnel wall, and continuously expanding, deforming, and peeling off towards the open face. Due to the heterogeneity of the sandstone tunnel, it ultimately results in asymmetrical floor cracking damage.
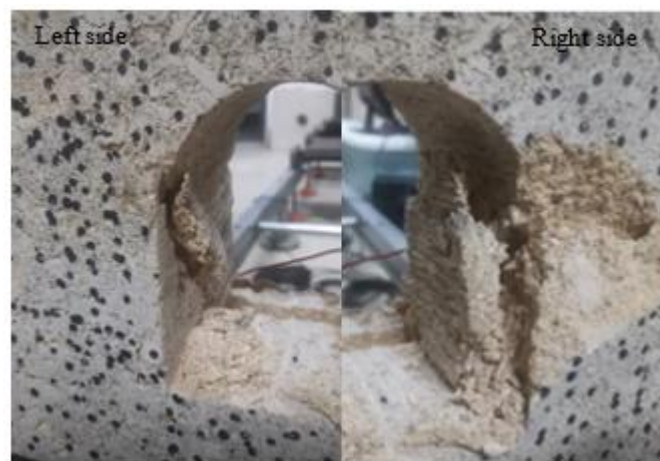

Figure 12. Photos of tunnel wall panel cracking and damage

5.2 Signs of Tunnel Failure

The extension of rock fractures follows a distinct fractal pattern. A fractal dimension close to 0 indicates that there are no cracks on the tunnel surface. A fractal dimension around 1 suggests that cracks of the tunnel surface tend to be distributed along a certain line. A fractal dimension close to 2 indicates that cracks almost cover the entire surface of the tunnel [11]. During the pore-closing and elastic deformation phases, the fractal dimension

gradually increases. A sudden increase in the fractal dimension indicates that the tunnel is about to fail before reaching its bearing capacity.

In the transition from crack extension to tunnel failure the acoustic emission b-value decreases rapidly and can serve as an early warning signal of tunnel failure. Shiotani et al. [17] applied acoustic emission technology to monitor the stability of rock slopes and found that the degree of fracture damage increased as the b-value decreased. Filipussi [18] observed that every macroscopic crack is accompanied by a rapid decrease of the b-value. The b-value reaches its minimum value when the crack specimen fails completely. Therefore, the b-value can be used as a predictive indicator of large-scale events during the rock fracture cracking process.

6. Conclusions

The tunnel wall initially develops tension cracks on both sides, followed by the development of shear cracks that propagate diagonally downwards towards the far end under bi-directional compressive loading. The tunnel suffers from asymmetrical damage, with rock mass peeling off on the right side and forming a V-shaped groove. The inside of the tunnel is damaged by panel cracking, resulting in the tunnel wall being cut into multiple layers of thin rock blocks parallel to the side wall and separating from the tunnel wall.

The fractal dimension of cracks of tunnel surface is closely linked to the crack extension process. When the fractal dimension increases to around 1, macroscopic cracks appear in the tunnel surface. As the fractal dimension increases rapidly, the tunnel cracks continue to expand, and when it approaches 2, the tunnel fails.

During the deformation process of the tunnel, the acoustic emission b-value constantly fluctuates between rising and falling. The acoustic emission counts and amplitudes are not active when entering the crack extension stage, and the acoustic emission activity suddenly increases after the crack extension stage.

Prior to the failure of a straight-walled arch tunnel, there will be early warning signs of a sudden increase in fractal dimension and decrease in b-value of cracks. The b-value of acoustic emission provides the earliest warning time, while the fractal dimension of cracks provides the latest warning time. These findings may help engineers and researchers to develop better monitoring and prediction methods for tunnel stability and safety.

Data Availability

The data used to support the findings of this study are available from the corresponding author upon request.

Conflicts of Interest

The authors declare that they have no conflicts of interest.

References

[1]   L. M. Zhang, Y. Cong, F. Z. Meng, Z. Q. Wang, P. Zhang, and S. Gao, "Energy evolution analysis and failure criteria for rock under different stress paths," *Acta Geotech.*, vol. 16, no. 2, pp. 569-580, 2021. https://doi.org/10.1007/s11440-020-01028-1.

[2]   L. M. Zhang, W. W. Chao, Z. Y. Liu, Y. Cong, and Z. Q. Wang, "Crack propagation characteristics during progressive failure of circular tunnels and the early warning thereof based on multi-sensor data fusion," *Geomech. Geophys. Geo-Energy Geo-Resour.*, vol. 8, Article ID: 172, 2022. https://doi.org/10.1007/s40948-022-00482-3.

[3]   F. Q. Gong, Y. Luo, X. B. Li, X. F. Si, and M. Tao, "Experimental simulation investigation on rockburst induced by spalling failure in deep circular tunnels," *Tunn. Undergr. Space Technol.*, vol. 81, pp. 413-427, 2018. https://doi.org/10.1016/j.tust.2018.07.035.

[4]   X. J. Zhang, D. Wang, C. Xiao, and H. C. Zhen, "Test of rockburst in straight-wall-top-arch roadways(tunnels) and its splitting and shearing failure analysis," *Rock and Soil Mechanics*, vol. 34, pp. 35-40, 2013.

[5]   H. Zhou, J. J. Lu, S. C. Hu, C. Q. Zhang, R. C. Xu, and F. Z. Meng, "Influence of curvature radius of tunnels excavation section on slabbing of hard brittle rockmass under high stress," *Rock Soil Mech.*, vol. 37, no. 1, pp. 140-146, 2016. https://doi.org/10.16285/j.rsm.2016.01.017-en.

[6]   P. Z. Pan, S. T. Miao, Z. H. Wu, and X. T. Feng, "Laboratory observation of spalling process induced by tangential stress concentration in hard rock tunnel," *Int J. Geomech.*, vol. 20, no. 3, Article ID: 04020011, 2020. https://doi.org/10.1061/(ASCE)GM.1943-5622.0001620.

[7]   A. Chmel and I. Shcherbakov, "A comparative acoustic emission study of compression and impact fracture in granite," *Int J. Rock Mech. Min. Sci.*, vol. 64, pp. 56-59, 2013. https://doi.org/10.1016/j.ijrmms.2013.08.025.

[8]   M. M. Hu, H. Zhou, Y. H. Zhang, C. Q. Zhang, Y. Gao, D. W. Hu, and J. J. Lu, "Acoustic emission monitoring on damage evolution of surrounding rock during headrace tunnel excavation by TBM," *Eur J. Environ Civ. Eng.*, vol. 23, no. 10, pp. 1248-1264, 2019. https://doi.org/10.1080/19648189.2017.1344153.

[9]   J. S. Kim, K. S. Lee, W. J. Cho, H. J. Choi, and G. C. Cho, "A comparative evaluation of stress–strain and acoustic emission methods for quantitative damage assessments of brittle rock," *Rock Mech. Rock Eng.*, vol. 48, pp. 495-508, 2015. https://doi.org/10.1007/s00603-014-0590-0.

[10] R. Das, R. Dhounchak, and T. N. Singh, "Analysis and prediction of brittle failure in rock blocks having a circular tunnel under uniaxial compression using acoustic Emission technique: Laboratory testing and numerical simulation," *Geo-Engineering*, vol. 12, no. 1, pp. 1-23, 2021. https://doi.org/10.1186/s40703-020-00136-x.

[11] R. D. Peng, H. P. Xie, and Y. Ju, "Computation method of fractal dimension for 2-D digital image," *J. China Univ. Min. Technol.,* vol. 33, no. 1, pp. 19-24, 2004.

[12] B. Gutenberg and C. F. Richter, "Frequency of earthquakes in California," *Bull. Seismol Soc. Am.*, vol. 34, no. 4, pp. 185-188, 1994. https://doi.org/10.1785/BSSA0340040185.

[13] L. M. Zhang, S. Q. Ma, M. Y. Ren, S. Q. Jiang, Z. Q. Wang, and J. L. Wang, "Acoustic emission frequency and b value characteristics in rock failure process under various confining pressures," *Chin J. Rock Mech. Eng.*, vol. 34, no. 10, pp. 2057-2063, 2015.

[14] W. D. Ortlepp and T. R. Stacey, "Rockburst mechanisms in tunnels and shafts," *Tunn. Undergr. Space Technol.*, vol. 9, no. 1, pp. 59-65, 1994. https://doi.org/10.1016/0886-7798(94)90010-8.

[15] C. D. Martin and R. Christiansson, "Estimating the potential for spalling around a deep nuclear waste repository in crystalline rock," *Int J. Rock Mech. Min. Sci.*, vol. 46, no. 2, pp. 219-228, 2009. https://doi.org/10.1016/j.ijrmms.2008.03.001.

[16] D. S. Cheon, S. Jeon, C. Park, W. K. Song, and E. S. Park, "Characterization of brittle failure using physical model experiments under polyaxial stress conditions," *Int J. Rock Mech. Min. Sci.*, vol. 48, no. 1, pp. 152-160, 2010. https://doi.org/10.1016/j.ijrmms.2010.10.001.

[17] T. Shiotani, M. Ohtsu, and K. Ikeda, "Detection and evaluation of AE waves due to rock deformation," *Constr. Build. Mater.*, vol. 15, no. 5-6, pp. 235-246, 2001. https://doi.org/10.1016/S0950-0618(00)00073-8.

[18] D. A. Filipussi, "Caracterización de daño por 'b-value' de eventos de emisión acústica en ensayos de rotura de roca andesita," *Matéria*, vol. 23, no. 2, 2018. https://doi.org/10.1590/s1517-707620180002.0404.